The radiative impact of water ice clouds from a reanalysis of Mars Climate Sounder data

AGU PUBLICATIONS

Geophysical Research Letters

RESEARCH LETTER

10.1002/2014GL060235

Key Points:
- Tropical clouds increase diurnally averaged temperatures at 10 Pa by 10–15 K
- Polar hoods have a small radiative impact due to low density-scaled opacities
- Stronger meridional overturning circulation increases polar warmings by 6–8 K

Correspondence to:
L. J. Steele,
liam.steele@open.ac.uk

Citation:
Steele, L. J., S. R. Lewis, M. R. Patel (2014), The radiative impact of water ice clouds from a reanalysis of Mars Climate Sounder data, *Geophys. Res. Lett.*, *41*, 4471–4478, doi:10.1002/2014GL060235.

Received 14 APR 2014
Accepted 11 JUN 2014
Accepted article online 18 JUN 2014
Published online 7 JUL 2014

The radiative impact of water ice clouds from a reanalysis of Mars Climate Sounder data

L. J. Steele[1], S. R. Lewis[1], and M. R. Patel[1]

[1] Department of Physical Sciences, The Open University, Milton Keynes, UK

Abstract The radiative impact of water ice clouds on the atmosphere of Mars is analyzed via a reanalysis of Mars Climate Sounder (MCS) temperature and ice opacity profiles. Polar hood clouds only have a small radiative impact, while tropical clouds increase diurnally averaged temperatures at the 10 Pa level by ~10–15 K. Cloud radiative heating strengthens the meridional overturning circulation, increasing temperatures in the polar warmings by ~6–8 K and temperatures in the tropics by ~2 K (due to increased dust mass). The positions and wind speeds of the tropical and high-latitude jets are also modified through changes to the meridional temperature gradients. An effective ice particle radius of $r_{eff} = 1.4\,\mu m$ produces temperatures around the aphelion cloud belt in close agreement to MCS temperature retrievals. For high-altitude tropical clouds during northern autumn, a better agreement is found using $r_{eff} = 0.8\,\mu m$.

1. Introduction

Recent observations and modeling studies have begun to reveal the importance of water ice clouds in terms of modifying the atmospheric temperature structure and circulation on Mars. For example, studies of temperature inversions observed by Mars Pathfinder and Mars Global Surveyor [*Magalhães et al.*, 1999; *Hinson and Wilson*, 2004] and surface temperature anomalies in Thermal Emission Spectrometer (TES) retrievals [*Wilson et al.*, 2007] all suggest that clouds have important roles to play, producing local heating and cooling depending on location and time of day.

Modeling studies using both 1-D microphysical models and Mars global climate models (MGCMs) have shown that cloud radiative effects can account for the observed temperature inversions [*Colaprete and Toon*, 2000] and intensify tides [*Hinson and Wilson*, 2004; *Kleinböhl et al.*, 2013]. Cloud radiative effects have also been shown to increase temperatures directly in the tropics, and indirectly over the poles through stronger meridional circulation [*Wilson et al.*, 2008; *Madeleine et al.*, 2012]. More recently, *Wilson and Guzewich* [2014] used both modeling and MCS data to reveal the relationship between water ice clouds and the tropical temperature structure.

However, as the radiative impact of clouds is dependent upon the location and time of day in which they form, the results of modeling studies will be affected by incorrect predictions of cloud locations and/or opacities. *Wilson et al.* [2008] overcame this problem by assimilating TES nadir temperature profiles into an MGCM that did not include radiatively active clouds and attributing the tropical temperature differences (compared to an experiment with identical dust but no thermal assimilation) to the presence of clouds. However, the results were limited by the vertical extent of the TES nadir temperature profiles (which only extend to ~40 km altitude), and processes other than clouds may be responsible for some of the temperature differences.

Here we investigate the radiative impact of clouds on the atmospheric temperature structure and circulation by using a data assimilation scheme to construct a four-dimensional time-space map of water ice opacities. This is used by the MGCM to produce the radiative forcing associated with clouds. This procedure allows clouds to be inserted into the model at the correct time and location, and with the correct opacity, producing the most realistic state from which to analyze cloud radiative effects. The resulting data set allows a detailed study of the atmospheric state that is not possible using observations or models alone. The increased vertical coverage of the MCS temperature retrievals compared to the TES retrievals allows the radiative effects of clouds to be studied to higher altitudes than has previously been possible. The results are also compared against an assimilation of MCS temperature profiles.

2. Data and Assimilation Method

2.1. Mars Climate Sounder Data

The temperature and ice opacity profiles are from the MCS instrument aboard the Mars Reconnaissance Orbiter spacecraft (version 3, level 2 retrievals on the Planetary Data System atmosphere node), which extend to an altitude of ~85 km, with a vertical resolution of ~5 km [*McCleese et al.*, 2010]. The observations comprise two sets of 12 strips of data per sol, separated by ~30° in longitude, and occur at local times around 3 A.M. and 3 P.M. away from the poles. The period chosen for study is Mars Year (MY) 30 (where MY follows the designation of *Clancy et al.* [2000]), as it comprises a more complete data set than other years, with ~1000–2500 profiles available for assimilation each sol. Retrievals are not included in this data set when the water ice opacity exceeds 0.004 km^{-1}, so there will be a slight bias toward lower opacity clouds.

Prior to assimilation the ice opacities per kilometer are multiplied by a factor of 3.1 to convert them from infrared wavelengths at 12 μm to visible wavelengths at 670 nm [*Kleinböhl et al.*, 2011]. These are then interpolated to obtain layer opacities, $d\tau_l$, on a set of 21 pressure levels, l, spaced 5 km apart and ranging from −10 km to 95 km (with the reference level of 610 Pa corresponding to $z = 0$ km).

2.2. Model and Assimilation Method

The MGCM used for this study results from a collaboration between the Laboratoire de Météorologie Dynamique (LMD), the University of Oxford, and The Open University. The model [see *Lewis et al.*, 2007] combines the most recent LMD physical schemes with a spectral dynamical core, an energy and angular-momentum conserving vertical finite-difference scheme, and a semi-Lagrangian advection scheme for tracers. Dust is free to be transported by the model using a two-moment scheme [*Madeleine et al.*, 2011], but the total dust optical depth in each column (and hence the dust mass and number mixing ratios in each layer) is scaled to match a total dust optical depth obtained from weighted binning and kriging of spacecraft data [*Montabone et al.*, 2014]. The model is run with a physical grid resolution of 5° in latitude and longitude, and there are 35 vertical levels in sigma coordinates, extending to an altitude of ~85 km. For the current study there is no water cycle included in the simulations, as we wish to analyze the radiative impact of clouds compared to a cloud-free atmosphere.

The data assimilation scheme is a modified form of the Analysis Correction (AC) scheme, originally developed for use at the UK Met Office [*Lorenc et al.*, 1991] and later retuned for Martian conditions [*Lewis et al.*, 1997] and verified using independent radio occultation data [*Montabone et al.*, 2006]. Temperature profiles are assimilated with the method used previously for TES assimilations, with temperatures compared in the form of layer thicknesses [see *Lewis et al.*, 2007]. For the ice opacity assimilation, the opacities in each profile are converted from observation levels l to model levels m (assuming the opacity varies linearly with $\ln p$), and then the opacity increment $\Delta\tau_m = d\tau_m^{\mathrm{obs}} - d\tau_m^{\mathrm{model}}$ is calculated. As the model is run without a water cycle, the $d\tau_m^{\mathrm{model}}$ term represents the previously assimilated data interpolated horizontally to the current observation location.

The background vertical correlations are approximated by a Gaussian function of the form

$$\mu_{ml}^{\mathrm{v}} = \exp\left[-\beta \ln^2(P_m/P_l)\right], \tag{1}$$

where P_m and P_l represent the pressures at the midpoints of layers m and l, and β is a dimensionless parameter. For this study we set $\beta = 8$. This form of the function has a relatively steep slope (which was chosen because ice clouds can form in shallow discrete layers) but still allows the spreading of data to one or more model levels.

Once the vertical assimilation step has been completed, the increments $\Delta\tau_m$ on each model level m are then spread horizontally to other model grid points using the method described in *Lewis et al.* [2007]. As the assimilated ice opacity field is not coupled to the model's water cycle, the ice opacity in a grid box no longer being updated by the assimilation scheme is decreased toward zero following a sinusoid with a relaxation time of 2 sols. This relaxation also helps to produce a diurnal variation in the ice opacities, which might not be accounted for by the assimilation process alone (due to the lack of local time variation in the observations). The true diurnal cycle is unlikely to be captured though, particularly in the tropics where daytime retrievals are sparse below ~50 Pa. This may affect the calculated heating rates and the resulting temperature field.

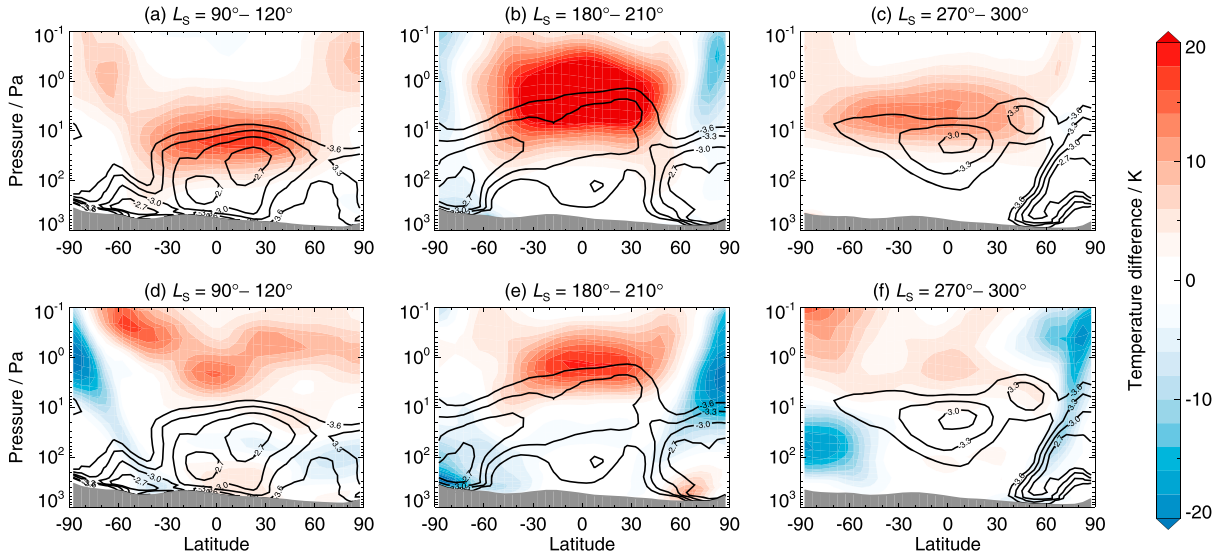

Figure 1. Time and zonal mean temperature differences (a–c) $T_{IA} - T_{CR}$ and (d–f) $T_{IA} - T_{TA}$ for three periods of MY 30. Black contours show $\log_{10}$ (infrared water ice opacity per kilometer) at −[3.6, 3.3, 3.0, 2.7] log units; compare with *McCleese et al.* [2010]. Grey shading represents topography.

With this procedure, the assimilation scheme is in essence being used to build a four-dimensional time-space map of water ice opacities which is used by the model to produce the radiative forcing associated with clouds. To calculate the single-scattering parameters required by the radiative transfer scheme, the effective radius, r_{eff}, and variance, v_{eff}, of the ice particle distribution need to be supplied. We use the same values used in the MCS radiative transfer scheme ($r_{eff} = 1.4\,\mu m$ and $v_{eff} = 0.15$ [see *Kleinböhl et al.*, 2011]), which were chosen as a compromise between the range of observed particle sizes.

2.3. Simulations Performed

Three simulations were performed to investigate cloud radiative effects. The initial conditions were obtained from a 6 year model spin-up from rest using the two-moment dust scheme, with the dust mass and number mixing ratios in each layer scaled by the *Montabone et al.* [2014] MY 30 dust scenario. The first is the control run (referred to hereafter as CR) in which dust and CO_2 are the only atmospheric constituents that are transported and influence the radiative transfer. Next, assimilations of MCS ice opacity profiles (referred to as IA for "ice assimilation") and temperature profiles (referred to as TA for "temperature assimilation") were performed using the same model and initial conditions as the CR. Comparison between the CR and IA allows the radiative impact of clouds to be investigated, while comparison between the IA and TA allows the performance of the IA and any remaining temperature biases to be assessed.

3. The Radiative Impact of Clouds

The impact of the assimilated clouds on atmospheric temperatures can be seen in Figures 1a–1c, which show the $T_{IA} - T_{CR}$ temperature differences. These three periods capture the main cloud features seen on Mars: the aphelion cloud belt (ACB) and the north and south polar hoods (SPH). The temperature changes are the result of both the direct radiative impact of clouds and the indirect impact caused by changes to the atmospheric circulation.

3.1. Direct Radiative Impact

In the tropics and midlatitudes there is an increase in temperature both at and above the cloud level. This increase is ~10–15 K during northern summer and winter (Figures 1a and 1c) but is > 30 K during northern autumn (Figure 1b). The increased heating in autumn is the result of the clouds in the tropics being located around 20 km higher compared to during northern summer. This results in larger density-scaled opacities, and it is this quantity which is related to heating rates [e.g., *Heavens et al.*, 2010]. The location of increased temperatures in the tropics between $L_S = 90°–120°$ is comparable to that found by *Wilson et al.* [2008] and *Madeleine et al.* [2012], though the peak temperature increase is ~5 K larger here. Additionally, while comparisons with TES retrievals in the *Wilson et al.* [2008] and *Madeleine et al.* [2012] studies only extend to

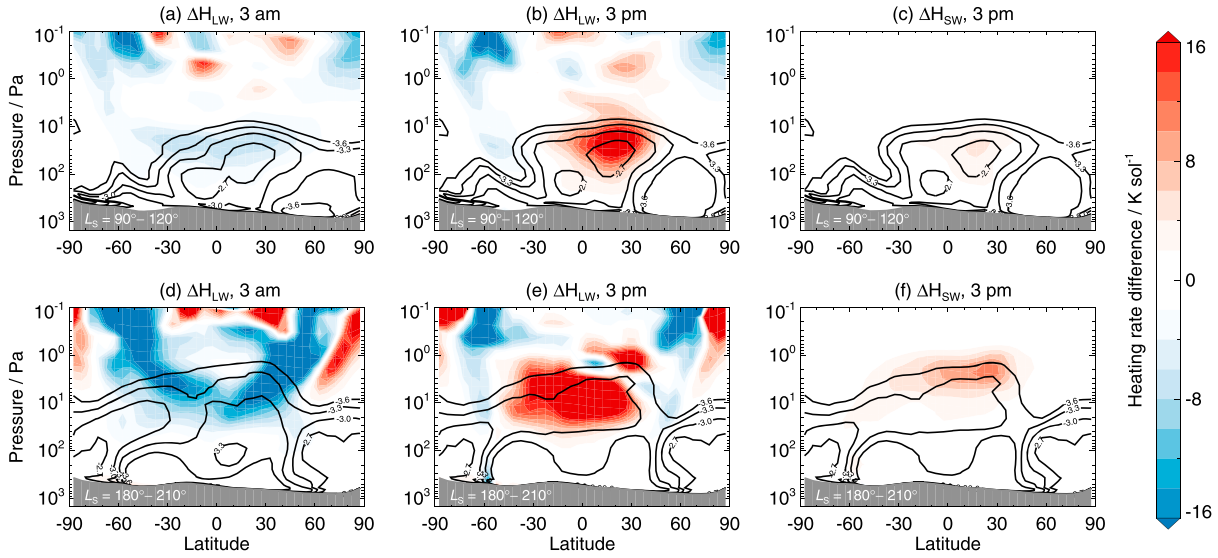

Figure 2. Time and zonal mean heating rate differences, $\Delta H = H_{IA} - H_{CR}$, around (a–c) northern summer and (d–f) autumn. Longwave differences are shown for both 3 A.M. and 3 P.M. (Figures 2a, 2b, 2d, and 2e), while shortwave differences are only shown for 3 P.M. (Figures 2c and 2f). Contours and grey shading as in Figure 1.

around 10 Pa, these results show that increased temperatures associated with clouds extend a further two pressure scale heights to around 1 Pa.

The polar hoods are generally the most optically thick clouds, but as can be seen in Figures 1b and 1c, they have very little impact on the local atmospheric temperature structure. During northern autumn the temperatures over the North Pole are only ~2–4 K cooler than in the simulation without clouds, and the temperature differences are even smaller during northern winter. At the South Pole there is a reduction in temperature of ~6–8 K caused by the SPH. The reason for the small radiative impact of the polar hoods is related to the low altitude at which they form (resulting in a small density-scaled opacity) and a smaller temperature difference between the surface and cloud-forming height (leading to less significant absorption of upwelling radiation). This is in contrast to the 10–15 K cooling caused by polar hoods in the simulation of *Madeleine et al.* [2012], which resulted from the clouds being too optically thick.

Figure 2 shows the heating rate difference between the IA and CR for the northern summer and autumn periods, and for 3 A.M. and 3 P.M. local times (longwave) and 3 P.M. only (shortwave). Tropical clouds produce local heating of ~10–30 K sol^{-1} during the day and cooling of ~5–10 K sol^{-1} at night (dependent on season and cloud thickness). Clouds also impact on shortwave heating (see Figures 2c and 2f), with daytime shortwave heating rates near the cloud tops peaking at ~5 K sol^{-1} in northern summer and ~10 K sol^{-1} in northern autumn.

3.2. Indirect Radiative Impact

While the temperature changes discussed above result mainly from the direct radiative effects of the clouds, there will also be a component related to the changing atmospheric circulation and the associated redistribution of other atmospheric constituents (in this case dust). For example, Figure 3 shows the mean meridional circulation that results from the IA (ψ_{IA}, contours) and the $\psi_{IA} - \psi_{CR}$ difference (shading). The inclusion of cloud radiative effects generally results in a strengthening of the overturning cells in each period, with a 50% increase in transport away from the centers of the cells, and peak increases approaching 200% in the upwelling and downwelling branches in Figures 3a and 3c. The strengthening of the Hadley cells causes dust in the tropics to be transported higher into the atmosphere. At 100 Pa (~20 km altitude), the dust mass mixing ratio is increased by around 40% in northern summer and between 5–10% in northern winter. This increased tropical dust mass is responsible for around 2 K of the tropical temperature increases shown in Figures 1a–1c.

As well as redistributing atmospheric constituents, the increasing strength of the meridional circulation also affects the strength of the polar warmings through increased adiabatic heating in the descending branch

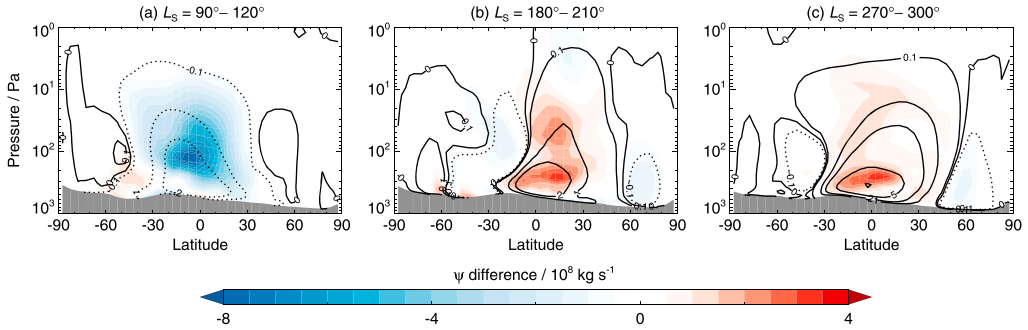

Figure 3. Mean meridional circulation, ψ, from the IA (black contours, 10^9 kg s^{-1}) and the $\psi_{IA} - \psi_{CR}$ difference (shading) for three different periods. The (solid, dotted) contours represent (clockwise, anticlockwise) circulation. Grey shading represents topography.

of the overturning cells. As can be seen in Figures 1a and 1c, the presence of clouds results in a temperature increase of ~6–8 K in the polar warmings. The impact of clouds during northern autumn is a slight equatorward shift of both the polar warmings. This results in the negative temperature differences seen over both poles above 10 Pa in Figure 1b and the heating rate difference pattern seen above 10 Pa in Figures 2d and 2e.

The temperature changes associated both directly and indirectly with clouds alter the meridional temperature gradients, leading (through the thermal wind relation) to changes in jet speeds. In the autumn and winter hemispheres the cores of the westerly jets are strengthened by ~10–20 m s^{-1}, while over the equator during northern autumn the easterly jet speed is reduced, with the core speed decreasing from > 100 m s^{-1} to ~40 m s^{-1}.

4. Comparison With an Assimilation of MCS Temperature Profiles

To study any biases in the IA temperature field, a comparison is made against the results of the TA. The $T_{IA} - T_{TA}$ temperature differences for the same three periods discussed previously are shown in Figures 1d–1f. The inclusion of cloud radiative effects produces tropical temperatures at cloud-forming height in the IA that are in much better agreement with the TA than the CR, with differences of only a few K. Above cloud-forming height, the general trend is for atmospheric temperatures in the IA to be too warm compared to the TA, particularly in Figure 1e where temperatures in the IA are ~10–20 K higher than in the TA. This excess heating is related to the constant particle size of $r_{eff} = 1.4$ μm used in the radiative transfer scheme. Tests using a variety of different r_{eff} values show that decreasing r_{eff} to 0.8 μm during autumn reduces the daytime heating rates and nighttime cooling rates to values in line with those shown in Figures 2a and 2b, giving results only ~2 K warmer than in the TA. Thus, the tropical clouds during autumn appear to be composed of smaller particles than the ACB.

The other main biases above cloud-forming height are the negative temperature differences over the South Pole in Figure 1d and over the North Pole in Figures 1e and 1f. These features (related to the polar warming) are also apparent in the free-running model and are not a direct result of cloud radiative effects. The inclusion of clouds improves the southern polar warming in Figure 1d through increased temperatures associated with a stronger meridional circulation, but the polar warming in the TA has more of a poleward tilt than in the CR or IA. While the magnitude of the polar warming in the Northern Hemisphere is improved by including cloud radiative effects, the tilt is altered, becoming more vertical than in the TA. This is the reason for the negative temperature differences in Figures 1e and 1f. The remaining temperature biases are present in both the IA and CR, and are not impacted by cloud radiative effects. The cold biases over the summer poles in Figures 1d and 1f and the low-level north polar warm bias in Figure 1e are related to the dust distribution in the model, while the upper atmosphere warm bias in Figure 1d is related to the modeled tides. These are not discussed further here, as the focus of this paper is on the radiative impact of clouds.

To investigate the performance of the IA outside the three periods discussed so far, the zonal mean 3 A.M. and 3 P.M. equatorial temperatures in the CR and IA were compared with the TA for the whole of MY 30 (the polar hoods were not investigated as they have little radiative impact). The $T_{IA} - T_{TA}$ results are shown in

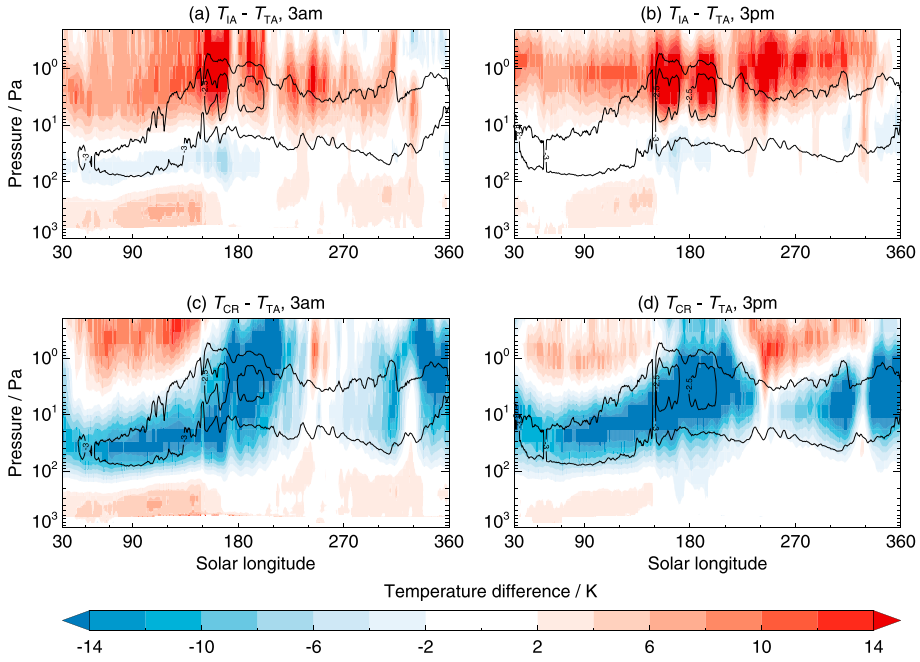

Figure 4. Zonal mean 3 A.M. and 3 P.M. temperature differences at the equator between the (a and b) IA and TA and the (c and d) CR and TA. Data are smoothed with a boxcar smoothing over 2° of L_S. Black contours show $\log_{10}$ (infrared density-scaled water ice opacity) at −3.5 and −2.5 log units.

Figures 4a and 4b and the $T_{CR} - T_{TA}$ results are shown in Figures 4c and 4d. Note that there are no MCS data available to assimilate until around $L_S = 20°$, and there is a 5 sol gap in the data around $L_S = 150°$.

It can be seen that there are cold biases of up to 20 K in CR which follow the locations of the assimilated clouds. The IA greatly improves the cold biases, with the best agreement with the TA occurring between ~10 and 100 Pa. There is little change in the temperature structure between the CR and IA below around 100 Pa. The warm biases at and above the cloud tops between $L_S = 150°$ and 360° (and particularly around $L_S = 180°$) are the result of the ice particle effective radius of 1.4 μm being too large. Better agreement with the TA is obtained when using $r_{eff} = 0.8$ μm for these high-altitude clouds. There is little change to the warm biases that can be seen in the CR above ~3 Pa between $L_S = 30°$–150° and $L_S = 230°$–330°, though the IA makes the biases slightly warmer due to the emission from clouds. These biases are not directly related to clouds and are possibly the result of an incorrect representation of tides.

Periods where the cold bias in the CR disappears (around $L_S = 240°$ and 330°) correspond to the presolstice and postsolstice dust storms. The convergence of the CR toward the TA shows that dust storms significantly reduce the impact of clouds on the atmospheric temperature. In the IA, temperatures are too warm during these periods. Taking the ice opacity observations to be correct, this may be because of a decrease of the ice particle size during the dust storms, which would result in reduced heating. Such a situation is not accounted for in the IA when using a constant ice particle effective radius of 1.4 μm.

It can also be seen in Figures 4a and 4b that the IA achieves a better agreement with the TA during the daytime than the nighttime. In particular, at 3 A.M. there is a cold bias centered at roughly 50 Pa between $L_S = 30°$ and 150°, revealing that the IA is too cold at this time. As described by *Wilson et al.* [2014], tide-induced vertical velocities between 20 and 100 Pa in the tropics are downward, resulting in adiabatic warming. This tide response is enhanced through cloud forcing [e.g., *Kleinböhl et al.*, 2013; *Wilson and Guzewich*, 2014], suggesting that thicker nighttime clouds are present than are included in the assimilation.

5. Conclusions

Assimilations of MCS temperature and ice opacity profiles have been performed to investigate the radiative impact of water ice clouds. Tropical clouds are shown to produce local daytime heating rates and nighttime cooling rates of ~10–20 K sol^{-1} and ~5 K sol^{-1}, respectively. The diurnally averaged result is an increase in

atmospheric temperatures by ~10–15 K at the 10 Pa level, broadly in agreement with the results of *Wilson et al.* [2008] and *Madeleine et al.* [2012]. This study extends above the 10 Pa level and shows that clouds directly increase tropical atmospheric temperatures up to around 1 Pa. An ice particle effective radius of 1.4 μm provides good results for the ACB radiative effects during the day, with temperatures in the IA only a few K different to the TA. For high-altitude tropical clouds during northern autumn, a better match with the TA occurs when using $r_{eff} = 0.8\,\mu m$, suggesting that these clouds are composed of smaller particles than the ACB. Thicker clouds are likely required to match the nighttime temperatures in the TA. Polar hood clouds only have a small radiative impact because of their low density-scaled opacities and less significant absorption of upwelling radiation.

Clouds also have an indirect effect on the atmosphere, with the strengthening overturning circulation increasing polar warming temperatures by ~6–8 K. Jet speeds are also modified by changes to the meridional temperature gradient. The cores of the winter westerly jets increase by ~10–20 m s^{-1}, while the equatorial easterly jet weakens by ~60 m s^{-1} (compared to a cloud-free atmosphere). The changing circulation also leads to the redistribution of atmospheric constituents, with increases in tropical dust amounts raising temperatures by ~2 K between 1 and 10 Pa.

While the radiative impact of clouds has led to improvements in the modeled atmospheric temperature structure, there are still some biases present. Many of these can be improved using different ice particle effective radii in the radiative transfer calculations, but some are related to the dust distribution and modeled tides. It should also be noted that the MCS retrievals assimilated here do not account for the most optically thick clouds, and this may play a role in the remaining temperature biases. Future work will make use of updated MCS retrievals and will couple the assimilation to a model including an active water cycle.

Acknowledgments
The authors acknowledge the support of the MCS science team and Luca Montabone and thank John Wilson for his suggestions which helped improve this paper. We are grateful for an ongoing collaboration with François Forget and coworkers at LMD. MCS data are archived in the Planetary Data System. Model results are available from the authors upon request. This work was funded by the UK Science and Technology Facilities Council.

The Editor thanks John Wilson and an anonymous reviewer for their assistance in evaluating this paper.

References

Clancy, R. T., B. J. Sandor, M. J. Wolff, P. R. Christensen, M. D. Smith, J. C. Pearl, B. J. Conrath, and R. J. Wilson (2000), An intercomparison of ground-based millimeter, MGS TES, and Viking atmospheric temperature measurements: Seasonal and interannual variability of temperatures and dust loading in the global Mars atmosphere, *J. Geophys. Res.*, *105*, 9553–9572, doi:10.1029/1999JE001089.

Colaprete, A., and O. B. Toon (2000), The radiative effects of Martian water ice clouds on the local atmospheric temperature profile, *Icarus*, *145*, 524–532, doi:10.1006/icar.2000.6364.

Heavens, N. G., J. L. Benson, D. M. Kass, A. Kleinböhl, W. A. Abdou, D. J. McCleese, M. I. Richardson, J. T. Schofield, J. H. Shirley, and P. M. Wolkenberg (2010), Water ice clouds over the Martian tropics during northern summer, *Geophys. Res. Lett.*, *37*, L18202, doi:10.1029/2010GL044610.

Hinson, D. P., and R. J. Wilson (2004), Temperature inversions, thermal tides, and water ice clouds in the Martian tropics, *J. Geophys. Res.*, *109*, E01002, doi:10.1029/2003JE002129.

Kleinböhl, A., J. T. Schofield, W. A. Abdou, P. G. J. Irwin, and R. J. de Kok (2011), A single-scattering approximation for infrared radiative transfer in limb geometry in the Martian atmosphere, *J. Quant. Spectrosc. Radiat. Transfer*, *112*, 1568–1580, doi:10.1016/j.jqsrt.2011.03.006.

Kleinböhl, A., R. J. Wilson, D. Kass, J. T. Schofield, and D. J. McCleese (2013), The semidiurnal tide in the middle atmosphere of Mars, *Geophys. Res. Lett.*, *40*, 1952–1959, doi:10.1002/grl.50497.

Lewis, S. R., M. Collins, and P. L. Read (1997), Data assimilation with a Martian atmospheric GCM: An example using thermal data, *Adv. Space Res.*, *19*, 1267–1270, doi:10.1016/S0273-1177(97)00280-9.

Lewis, S. R., P. L. Read, B. J. Conrath, J. C. Pearl, and M. D. Smith (2007), Assimilation of thermal emission spectrometer atmospheric data during the Mars Global Surveyor aerobraking period, *Icarus*, *192*, 327–347, doi:10.1016/j.icarus.2007.08.009.

Lorenc, A. C., R. S. Bell, and B. MacPherson (1991), The Meteorological Office analysis correction data assimilation scheme, *Q. J. R. Meteorol. Soc.*, *117*, 59–89, doi:10.1002/qj.49711749704.

Madeleine, J.-B., F. Forget, E. Millour, L. Montabone, and M. J. Wolff (2011), Revisiting the radiative impact of dust on Mars using the LMD Global Climate Model, *J. Geophys. Res.*, *116*, E11010, doi:10.1029/2011JE003855.

Madeleine, J.-B., F. Forget, E. Millour, T. Navarro, and A. Spiga (2012), The influence of radiatively active water ice clouds on the Martian climate, *Geophys. Res. Lett.*, *39*, L23202, doi:10.1029/2012GL053564.

Magalhães, J. A., J. T. Schofield, and A. Seiff (1999), Results of the Mars Pathfinder atmospheric structure investigation, *J. Geophys. Res.*, *104*, 8943–8955, doi:10.1029/1998JE900041.

McCleese, D. J., et al. (2010), Structure and dynamics of the Martian lower and middle atmosphere as observed by the Mars Climate Sounder: Seasonal variations in zonal mean temperature, dust, and water ice aerosols, *J. Geophys. Res.*, *115*, E12016, doi:10.1029/2010JE003677.

Montabone, L., S. R. Lewis, P. L. Read, and D. P. Hinson (2006), Validation of Martian meteorological data assimilation for MGS/TES using radio occultation measurements, *Icarus*, *185*, 113–132, doi:10.1016/j.icarus.2006.07.012.

Montabone, L., F. Forget, E. Millour, R. J. Wilson, S. R. Lewis, D. Kass, A. Kleinböhl, M. T. Lemmon, M. D. Smith, and M. J. Wolff (2014), Eight Martian years of dust climatology reconstructed from spacecraft observations, paper presented at Fifth International Workshop on the Mars Atmosphere: Modeling and Observations, CNRS, Oxford, U. K.

Wilson, R. J., and S. D. Guzewich (2014), Influence of water ice clouds on nighttime tropical temperature structure as seen by the Mars Climate Sounder, *Geophys. Res. Lett.*, *41*, 3375–3381, doi:10.1002/2014GL060086.

Wilson, R. J., G. A. Neumann, and M. D. Smith (2007), Diurnal variation and radiative influence of Martian water ice clouds, *Geophys. Res. Lett.*, *34*, L02710, doi:10.1029/2006GL027976.

Wilson, R. J., S. R. Lewis, L. Montabone, and M. D. Smith (2008), Influence of water ice clouds on Martian tropical atmospheric temperatures, *Geophys. Res. Lett.*, *35*, L07202, doi:10.1029/2007GL032405.
Wilson, R. J., E. Millour, T. Navarro, F. Forget, and M. Kahre (2014), GCM Simulations of aphelion season tropical cloud and temperature structure, paper presented at Fifth International Workshop on the Mars Atmosphere: Modeling and Observations, CNRS, Oxford, U. K.